



Geophysical Research Letters*



RESEARCH LETTER

10.1029/2024GL110222

Key Points:

- Seismic imaging suggests a Main Himalayan Thrust-associated lowvelocity channel with north-dipping anisotropic foliation
- Modeling of InSAR and GNSS data together suggests a weak channel with anisotropic rigidity whose orientation matches seismic constraints
- The weak anisotropic plate boundary may be related to S-C fabrics and influence the margin geodynamics on different time scales

Supporting Information:

Supporting Information may be found in the online version of this article.

Correspondence to:

S. Li, shaoyangli@mail.iggcas.ac.cn

Citation:

Li, S., Schulte-Pelkum, V., Barnhart, W. D., Chen, L., Karplus, M., & Oncken, O. (2024). Weak, vertically stronger Main Himalayan Thrust in the India-Asia collision. *Geophysical Research Letters*, 51, e2024GL110222. https://doi.org/10.1029/2024GL110222

Received 9 MAY 2024 Accepted 12 AUG 2024

Weak, Vertically Stronger Main Himalayan Thrust in the India-Asia Collision

Shaoyang Li¹, Vera Schulte-Pelkum^{2,3}, William D. Barnhart^{4,5}, Ling Chen^{1,6}, Marianne Karplus⁷, and Onno Oncken⁸

¹State Key Laboratory of Lithospheric and Environmental Coevolution, Institute of Geology and Geophysics, Chinese Academy of Sciences, Beijing, China, ²Cooperative Institute for Research in Environmental Sciences, University of Colorado Boulder, Boulder, CO, USA, ³Department of Geological Sciences, University of Colorado Boulder, Boulder, CO, USA, ⁴Department of Earth and Environmental Sciences, The University of Iowa, Iowa City, IA, USA, ⁵Now at Earthquake Hazards Program, U.S. Geological Survey, Golden, CO, USA, ⁶College of Earth and Planetary Sciences, University of Chinese Academy of Sciences, Beijing, China, ⁷Department of Geological Sciences, University of Texas at El Paso, El Paso, TX, USA, ⁸Helmholtz Centre Potsdam, GFZ German Research Centre for Geosciences, Potsdam, Germany

Abstract Megathrusts at convergent plate boundaries generate the largest and some of the most hazardous earthquakes on Earth. However, their physical properties, including those influencing fault slip accumulation and release and earthquake-related surface displacements, are still poorly constrained at critical depths. Here, we combine seismic imaging and geodetic modeling to investigate the structure and mechanical behavior of the Main Himalayan Thrust fault (MHT) in the center of the 2015 Mw 7.8 Gorkha rupture in Nepal. Our results from two independent observations consistently suggest the presence of a channel associated with the MHT with high compliance (shear modulus as low as ~4 GPa) and strain anisotropy (stiffer in the vertical orientation than in the horizontal), likely arising from a weak subducting layer with north-dipping foliation. Such mechanical heterogeneity significantly influences the quantification of short-term fault kinematics and associated earthquake potential, with implications on across-scale dynamics of plate boundaries in Himalaya and elsewhere.

Plain Language Summary The Main Himalayan Thrust fault marks the boundary where the Indian continent slides beneath the Eurasian plate, causing earthquakes like the 2015 magnitude 7.8 event in Nepal. Subsurface images constructed using seismic waves suggest a weak layer surrounding the fault. However, we show that the seismic signature of this layer changes depending on the direction in which the seismic waves travel through it. We compare this information on the subsurface structure to insights from static surface motions during the earthquake. We find that the fit to the motion is poor when we assume the subsurface rock around the fault has the same strength in both horizontal and vertical orientations. The fit improves when we assume the near-fault rock is stronger under vertical compression than under horizontal compression. This assumption also helps explain the images constructed using seismic waves. We suggest that a strong oriented rock fabric develops in a channel around the plate boundary. The presence of this fabric may have influenced our estimates of fault slip before, during and after great earthquakes. Accurately describing this behavior is crucial for understanding the earthquake potential of plate boundary faults.

1. Introduction

The collision between the Indian and Asian continental plates has driven crustal shortening, thickening, and orogeny in the Himalaya and Tibetan Plateau since ~50–60 Ma (Hodges, 2000; Kapp & DeCelles, 2019; Yin & Harrison, 2000). Active thrust faults at the collision front are inferred to sole into a common low-angle detachment thrust fault named the Main Himalayan Thrust (MHT) (Ader et al., 2012; Yin, 2006). This fault is suggested to be mechanically weak based on the background microseismicity and force balance (Bollinger et al., 2004; Dielforder et al., 2020). It hosts megathrust earthquakes that accommodate, in part, the convergence in the locked zone of the megathrust fault (Ader et al., 2012; Bilham et al., 2001) and is thought to contribute to mountain building in the Himalaya (Avouac, 2015; Dal Zilio et al., 2021). Given these relationships, the interplay between geologic structure, mechanical properties, and seismic cycles on the MHT is crucial for understanding both earthquake processes and long-term orogenic processes operating on distinct time scales. The 2015 Mw 7.8 Gorkha, Nepal earthquake is the first event of its size in the Himalayan arc captured with modern high-resolution

© 2024. The Author(s). This is an open access article under the terms of the Creative Commons Attribution License, which permits use, distribution and reproduction in any medium, provided the original work is properly cited.

seismological and space-geodetic instruments (Avouac et al., 2015; Bilham, 2019; Galetzka et al., 2015), presenting an unprecedented opportunity to explore in detail the kinematic and mechanical properties of the MHT. The event ruptured an area of the MHT that was traversed previously (Figure 1a) by densely spaced temporary broadband seismic stations of the HICLIMB network (Nábělek et al., 2009), which interpreted a near-horizontal interface capped by a low-velocity zone (Figure 1b) (Duputel et al., 2016; Hetényi et al., 2010; Nábělek et al., 2009). Results from the sparser HIMNT temporary network (Sheehan et al., 2001), slightly to the east of the main HICLIMB line, found that the MHT signature is strongly backazimuth-dependent, interpreted as anisotropy in a several km thick layer with a foliation that dips more steeply north relative to the gently dipping to subhorizontal MHT trace (Figure 1b) (Schulte-Pelkum et al., 2005). Whether such anisotropy is also present in the low-velocity layer crossing the source region of the 2015 event (Figure 1a) was not investigated in previous work (Duputel et al., 2016; Hetényi et al., 2010; Nábělek et al., 2009) with HICLIMB stations.

Since seismic velocities can in theory be directly related to elastic mechanical rock properties (Jaeger et al., 2009), low seismic velocity and seismic anisotropy associated with the MHT would affect its mechanical behavior during earthquake deformation processes. Coseismic deformation of the 2015 Gorkha earthquake, derived from interferometric synthetic aperture radar (InSAR) and global navigation satellite systems (GNSS), have been extensively studied in previous geodetic studies with a focus on source characteristics (e.g., Elliott et al., 2016; G. Feng et al., 2015; W. Feng et al., 2017; Grandin et al., 2015; McNamara et al., 2017; Qiu et al., 2016; K. Wang & Fialko, 2015). Common elements in these studies are that inversions invoked assumptions of a homogeneous elastic halfspace and a zero-thickness fault interface as a sharp boundary between two tectonic units. Observed deformation is thus entirely attributed to the inverted earthquake source and sometimes the variation of fault geometry (Elliott et al., 2016; Qiu et al., 2016), while the MHT channel (as seismically constrained) and its importance on kinematics and dynamics in the Himalayan arc have been geodetically unexplored.

Although previous studies fit the co-seismic horizontal GNSS displacements and InSAR line-of-sight (LOS) displacements reasonably well, the studies invoke varying degrees of fault geometry complexity and slip distribution complexity within a homogeneous elastic halfspace Earth model. In source models with a simplified, single plane fault geometry, such as those described in McNamara et al. (2017) and Hayes et al. (2015), distributed slip inversions re-predict InSAR observations well but systematically underpredict the horizontal displacements. Subsequent studies in part overcame this discrepancy through the imposition of spatially varying fault geometries within a homogeneous elastic halfspace Earth model (e.g., Elliott et al., 2016; Qiu et al., 2016). This study focuses on the role seismically constrained, depth-varying material properties, as opposed to fault geometry, may serve in resolving discrepancies between the fits to horizontal and LOS displacements.

We combine seismic imaging and geodetic modeling to investigate the physical properties and mechanical behavior of the MHT channel. We first investigate the seismic structural signal from receiver function analysis (Figure 1b, case D and E) in terms of the presence of an isotropic low-velocity channel, an anisotropic layer, or both. We then assemble InSAR and GNSS observations (Figure 1b, case A and B) to constrain coseismic vertical and horizontal displacements. We conduct 2D finite-element modeling of coseismic displacements considering structural constraints from seismology. We find that we can jointly fit the GNSS and InSAR observations with a seismogenic fault surrounded by a low velocity channel that is stronger in the vertical orientation than in the horizontal orientation. This result indicates that geodetic observations may be capable of constraining compliance and mechanical anisotropy in concert with seismological approaches that constrain seismic velocity changes and wave anisotropy. Finally, we discuss the potential implications of such mechanical structure on the kinematics and dynamics at convergent plate boundaries and the geologic origins of the strain anisotropy.

2. Data and Methods

2.1. Time-Domain Receiver Function Analysis

Receiver function analysis has been reported for the isotropic velocity and signal polarity of the MHT in Nepal (e.g., Duputel et al., 2016; Nábělek et al., 2009; Schulte-Pelkum et al., 2005; Text S1 in Supporting Information S1). The time-domain method of receiver functions introduced by Ligorría and Ammon (1999) preserves absolute receiver function amplitude, expressed as the amplitude ratio between the vertical and horizontal component of a phase, which is relevant to our subsequent analysis. We use all available broadband data from the HICLIMB (2002–2005; 191 stations) (Nabelek, 2002), HIMNT (2001–2003; 31 stations) (Sheehan et al., 2001), and NAMASTE (2015–2016; 49 stations) (Karplus et al., 2020) networks (Figure 1a). The Gaussian filter factor

LI ET AL. 2 of 13

1944/8007, 2024, 16, Downloaded from https://agupubs.onlinelibrary.wiley.com/doi/10.1029/2024GL110222, Wiley Online Library on [26/08/2024]. See the Terms and Conditions (https://onlinelibrary.wiley.com/terms-and-conditions) on Wiley Online Library for rules of use; OA articles are governed by the applicable Creative

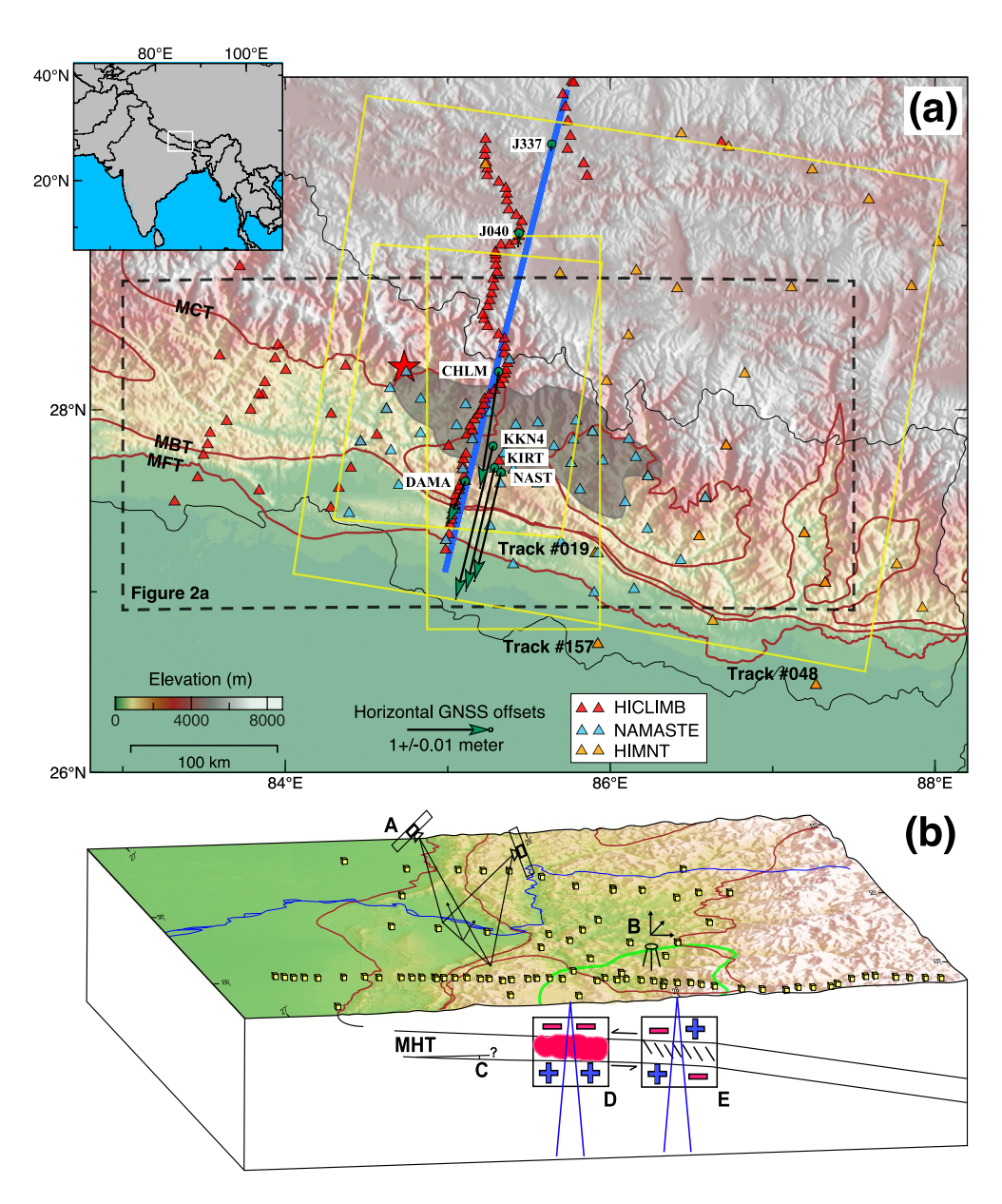


Figure 1. Map of the study area and conceptual sketch of geodetic and seismic observations. (a) Inset shows location in a broader geographic context. The red star shows Gorkha mainshock epicenter and the gray shading represents the Gorkha rupture limit from Mencin et al. (2016). Three InSAR tracks are shown by yellow rectangles and horizontal GNSS offsets are shown as black vectors with green arrowheads. The thick blue line indicates the model profile. (b) Top surface shows topography for part of the study area from the dense seismic station line eastward (cubes represent seismic stations), viewed from the East. The light green outline marks the Gorkha rupture from Mencin et al. (2016). Drawing is not to scale. (A) is a sketch InSAR ascending (left one) and descending (right one) satellite sensitivity for coseismic deformation along line-of-sight (black arrows), predominantly vertical. (B) is a sketch of a GNSS station recording horizontal and vertical coseismic deformation. (C) symbolizes previously inferred dips of the MHT (most publications prefer near 7° dip, but ramp-flat-ramp geometries with 0° dip on the flat portion have also been proposed). (D) sketches the polarity (positive and negative) of receiver function arrivals from the bottom and top of a horizontal to gently dipping low-velocity layer associated with the MHT; blue lines indicate rays incident from different teleseismic backazimuths. (E) sketches polarity of receiver function arrivals from an anisotropic layer associated with the MHT. A mix of cases D and E is also possible.

used is 3, resulting in a receiver function pulse width of roughly 1 s. Radial and transverse component receiver functions are calculated for teleseismic P, Pdiff, and PP phases for all events with magnitude of 5.0 or greater at epicentral distances of 28° minimum. The inclusion of Pdiff and PP phases does not change the appearance of the receiver functions and improves backazimuthal event coverage. We apply an automated quality control that

LI ET AL. 3 of 13

selects events by criteria for signal-to-noise ratio, variance reduction, maximum amplitude, pulse length, and characteristics of the radial component direct P pulse as described in detail by Schulte-Pelkum and Mahan (2014). An average of 22% of radial traces and 14% of transverse traces per station are retained after quality control.

At each station, we conduct the same workflow of receiver function analysis. We see the large radial component amplitude arrivals with changes in polarity within the first 2 s of receiver function at each station (e.g., Figures S1a and S1f in Supporting Information S1). Polarity flips on the radial component occur at roughly East (90°) and West (270°) backazimuths. The same arrivals are accompanied by large amplitudes on the transverse component (Figures S1b and S1g in Supporting Information S1) with polarity flips near North (0°) and South (180°). Neither observation is consistent with a subhorizontal to gently dipping low velocity layer. We process both components (Figures S1c, S1d, S1h, S1f in Supporting Information S1) to isolate the matching degree-1 harmonic signal (360° periodicity in backazimuth; Figures S1e and S1j in Supporting Information S1) using steps detailed in Schulte-Pelkum et al. (2020). We obtain the azimuthally varying portion of the radial component by subtracting the azimuthally invariant signal from each radial component trace (e.g., Figures S1c and S1h in Supporting Information S1). Theoretical results (Park & Levin, 2016) and synthetic models (Jones & Phinney, 1998; Savage, 1998; Schulte-Pelkum & Mahan, 2014) show that azimuthally varying 360°-periodic conversions from contrasts in plunging axis anisotropy or dipping interfaces have a 90° shift in backazimuth on the transverse component compared to the radial component, and the transverse receiver functions are azimuth-shifted accordingly (e.g., Figures S1d and S1i in Supporting Information S1). The two corrected components binned together (e.g., Figures S1e and S1j in Supporting Information S1) display the combined 360°-periodic signal with maximal azimuthal coverage thanks to the shifted transverse component signal. We apply a moving window of 0.25 s length and decompose the signal using backazimuthal harmonics with degrees 0, 1, and 2 (Schulte-Pelkum & Mahan, 2014). Because of biased sampling of illumination azimuths by global seismicity, a straightforward stack of all receiver functions may alias some of the azimuthally varying signal into an apparent azimuthally invariant signal. To separate the influence of isotropic layering from anisotropic contrasts, we stack averages of azimuthal bins to minimize a sampling bias. We also apply methods that explicitly target conversions from anisotropic contrasts (e.g., Schulte-Pelkum et al., 2020).

2.2. Finite-Element Modeling of Geodetic Data

In this study, we train our geodetic deformation models by combining InSAR data, which are generally more sensitive to the vertical displacements (Figure 1b, case A), and GNSS data, which are more sensitive to the horizontal displacements (Figure 1b, case B). We compile all 7 available stations from both continuous and survey modes along our trench-normal model profile (Figure 1a in map view and Figure S2 in Supporting Information S1 in profile view in Supporting Information), published by Galetzka et al. (2015), Wu et al. (2016), and Yadav et al. (2017). The GNSS offsets contain both horizontal and vertical components. In addition, we assemble an InSAR data set (Figure S3 in Supporting Information S1), which is derived from the ALOS-2 and Sentinel-1 missions and includes two descending and one ascending tracks, published by Hayes et al. (2015), Lindsey et al. (2015), and McNamara et al. (2017) (Table S1 in Supporting Information S1). Together, this data set contains three independent look angles of LOS (line of sight) displacements. Compiling geodetic data is described more thoroughly in Text S2 in Supporting Information S1. Due to the dense distribution of InSAR data and sparse distribution of GNSS data in space, we will use InSAR data to invert for fault slip distribution and then use GNSS data to evaluate the performance of forward simulations.

We build two-dimensional finite-element models across the main source region with respect to the available seismic and geodetic instrumentation (blue line in Figure 1a). All finite-element computations are conducted using the open-source software PyLith (Aagaard et al., 2013). More details on model setups are described in Text S2 in Supporting Information S1. To compare modeling results, we define a reference model with uniform elastic properties (μ of 30 GPa and ν of 0.25) for the entire model domain (named the REF model). In contrast to the REF model, we construct a model with only a weak subduction channel (layer), a model with only a compliant upper plate, and a model with both compliant upper and lower plates (Figure S6 in Supporting Information S1) to separately explore the contribution of the channel, upper plate (prism) and lower plate on the horizontal and vertical coseismic surface displacements. Given the very sparse GNSS observations, we purposely simplify these models by ignoring the topography and small-scale heterogeneities. In the weak-channel model, we assume a low-velocity channel with a uniform thickness of 8 km with the faulting plane in the middle (Figure S6a in Supporting Information S1) based on the 5–10 km low-velocity layer proposed by previous seismic imaging

LI ET AL. 4 of 13

studies (Duputel et al., 2016; Nábělek et al., 2009). We do not aim for a geodetic determination of both the thickness and mechanical properties of the weak layer and are mindful of the potential trade-off between them (i.e., the thinner the weaker the channel, and vice versa). We systematically vary the two elastic parameters of the weak bodies, according to their relationships with seismic velocities (Jaeger et al., 2009) $\mu = \rho V_S^2$ and $\nu = \frac{V_S^2 - 2V_P^2}{2(V_P^2 - 2V_S^2)}$, in which ρ , V_S , and V_P are density, P wave velocity, and S wave velocity, respectively. Each variation of the elastic parameters forms one finite-element model.

For each model with different elastic properties, we perform both forward and inverse modeling, following the workflow of Li and Barnhart (2020). First, we use each model to generate Green's functions by combining forward finite-element simulations of fault impulse (Masterlark, 2003) and an analytical bilinear orbit ramp function (Wright et al., 2004). Next, we use these Green's functions to invert the profiles of the three InSAR tracks (Figure S3 in Supporting Information S1) simultaneously for the fault slip distribution and the ramp signal of the InSAR data. The optimal slip of each model is determined from the optimal smoothing factor by selecting the inflection point of the L-shaped trade-off curves between data fit and model roughness (Bürgmann et al., 2005). We apply the same inversion constraints (e.g., the smoothing factor) for all the models and any variations between determined slip distributions thus depend solely on the variations of elastic properties specified in the weak body. Finally, we impose these slip distributions back into the original models and forward simulate the surface horizontal and vertical displacements. We evaluate the model performance by calculating the root-mean-square misfit (*RMS*, formula 1).

RMS =
$$\sqrt{\frac{1}{n} \sum_{j=1}^{n} (d_{\text{obs}}^{j} - d_{\text{mod}}^{j})^{2}}$$
 (1)

where n is the total number of GNSS sites, and d_{obs}^{j} and d_{mod}^{j} are the GNSS observed displacement and model-predicted displacement at the jth site, respectively. By performing the above workflow, we systematically assess the impacts of the weak bodies on horizontal and vertical displacements and investigate the geodetic signatures of the MHT as a weak layer.

3. Results and Discussion

3.1. Seismically Low-Velocity and Anisotropic MHT Layer Constrained From Receiver Functions

A double peak in A1 is visible at two representative stations (Figure S1 in Supporting Information S1), somewhat earlier at station NP035 closer to the Main Frontal Thrust (Figure 2a). The timing of the double peak corresponds to depths of arrivals previously interpreted as the MHT (Duputel et al., 2016; Nábělek et al., 2009; Schulte-Pelkum et al., 2005). There is no large amplitude A1 signal at zero delay time, unlike what would be expected in the presence of a dipping interface between isotropic layers (Schulte-Pelkum & Mahan, 2014). A shallowly dipping interface also does not generate the polarity flips in the radial component observed in the data (Figures S1a and S1f and Text S3 in Supporting Information S1). These factors point to anisotropy rather than interface dip as the cause for the A1 arrivals.

Polarity flips are \sim E-W (90° and 270°) for the earlier and later arrival at both stations (Figure S1 in Supporting Information S1), interpreted as \sim E-W oriented orogen-parallel foliation (Brownlee et al., 2017). They would match N-dipping fast foliation planes with a slow symmetry axis; an alternative option is a fast axis symmetry aligned lineation plunging to N lying within a N-dipping foliation plane (Schulte-Pelkum et al., 2020). Both geometries are consistent with top-to-the-south shear in the MHT layer. In upper crustal materials, a slow symmetry axis is more likely (Brownlee et al., 2017). Nevertheless, some other stations show some possible signals from upper crust materials (Text S3 in Supporting Information S1).

Figure 2a shows the largest A1 arrival from a depth range of 5–25 km at each station in the HICLIMB, HIMNT, and NAMASTE networks in the vicinity of the Gorkha rupture area. Large amplitudes are seen in the downdip (northern) vicinity of surface fault traces. The phase at each A1 maximum points in the direction of the maximum positive amplitude, with the polarity flips 90° from it in either direction. The latter corresponds to the strike of dipping subsurface foliation at a contrast (Brownlee et al., 2017). The majority of strikes point subparallel to the surface faults and trend of the orogen.

LI ET AL. 5 of 13

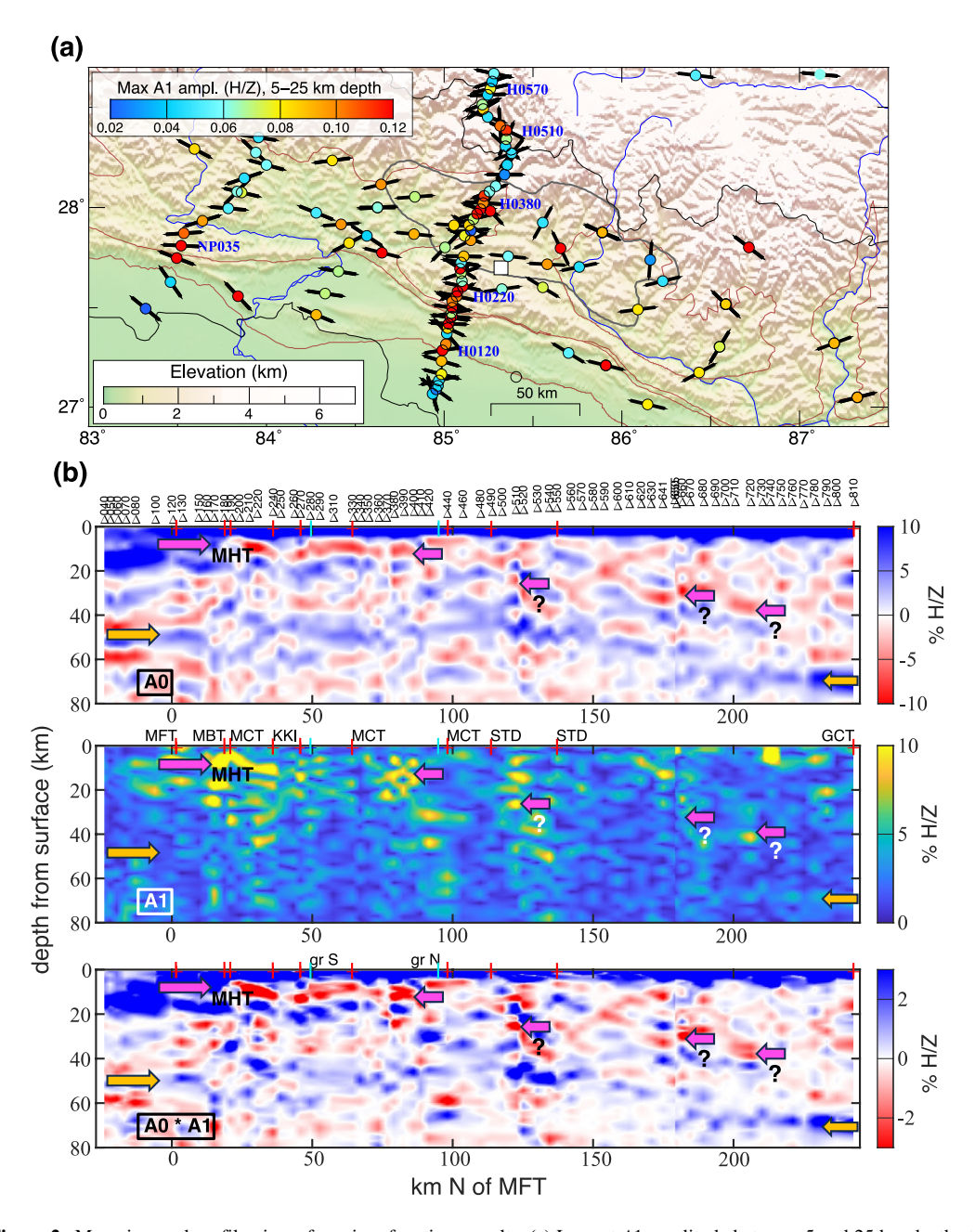


Figure 2. Map view and profile view of receiver functions results. (a) Largest A1 amplitude between 5 and 25 km depth at each seismic station. Black bars represent backazimuths of receiver function polarity flips at depth indicated by color, interpreted as strikes of dipping subsurface foliation. Some stations are labeled in blue for orientation. Gray outline marks the Gorkha rupture limit from Mencin et al. (2016). White square is Kathmandu. (b) Station-averaged receiver function traces for the dense line of stations near 85°E scaled to depth. (Top panel) Azimuth-averaged radial component receiver function A0, plotted under each station after stacking in azimuthal bins and averaging over bins. Amplitude color scale is percent horizontal to vertical component absolute amplitude of the time-domain receiver function. Triangles mark station locations and elevations with vertical exaggeration. Numbers above triangles are station codes (preceded by H0). Red and cyan tick marks are fault crossings and southern (grS) and northern (grN) Gorkha rupture extents labeled in subsequent panels. Bold MHT label marks the left end of the red-over-blue signature interpreted as MHT by Duputel et al. (2016). Magenta arrows trace possible MHT signature across profile. Orange arrows outline Moho arrival. (Middle panel) First azimuthal harmonic amplitude A1. Yellow features show high A1 amplitude. KK1 - Kathmandu Klippe; STD - South Tibetan Detachment fault; GCT - Great Counter Thrust. (Bottom panel) Product of A0 and A1, highlighting negative and positive A0 arrivals that are accompanied by a large A1 amplitude. MHT signature is amplified relative to other arrivals. Note that depth is relative to surface in order to show the entire waveform.

LI ET AL. 6 of 13

To determine which features show truly azimuthally invariant or variable components, we plot profiles of the radial component azimuthal bin average R0 as a proxy for azimuthally invariant A0, as well as the 360° -periodic A1 solution, in Figure 2b. The negative-over-positive signature persists in the A0 profile (top panel of Figure 2b), suggesting that there is indeed an isotropic subhorizontal low velocity layer associated with the MHT at \sim 25–80 km profile distance, which encompasses nearly all of the Gorkha mainshock rupture and a section south of it, consistent with the <10 km thick low-velocity zone inferred by Duputel et al. (2016). High amplitudes in A1 are seen in the same area (middle panel of Figure 2b) and overlap some of the A0 MHT signal, especially at depths similar to the upper interface with negative arrivals in A0 (bottom panel of Figure 2b).

3.2. Geodetic Signatures of High Compliance and Strain Anisotropy of the MHT

Before geodetically investigating the MHT channel, we conduct sensitivity tests of MHT geometry (Figure 1b, case C) on predicting surface deformation. The results suggest that the geometry variation is likely insufficient to jointly explain the GNSS data in horizontal and vertical directions under our 2D approximation of the collision system (Text S4 in Supporting Information S1). We then assume a fault geometry widely used in previous geodetic modeling studies of the high-quality coseismic and postseismic deformation of the 2015 Gorkha earthquake and focus on exploring the mechanical properties of MHT, considering our and previous seismic imaging results (e.g., Duputel et al., 2016; Schulte-Pelkum et al., 2005; Figure 2). In addition to the MHT channel, we also investigate the effects of the elastic properties of upper and lower plates on surface deformation and their contributions on fitting the near and far field GNSS data (Text S4 in Supporting Information S1).

Involving such a weak layer of the MHT in the finite-element models leads to a systematic variation of the optimally inverted fault slip (Figure S14 in Supporting Information S1) with the same optimal smoothing factor (Figure S15 in Supporting Information S1). A clear trade-off between the μ and the maximum slip is found. That is, a lower μ results in a higher maximum slip. Text S4 in Supporting Information S1 describes more on the results of the inverted fault slip. It suggests that the layer, if present, provides a first-order control on the magnitude and pattern of geodetically determined fault slip, despite the vertical GNSS and InSAR displacements being relatively insensitive to the weak layer (Figure 3c and Figure S16 in Supporting Information S1).

Our isotropic model results confirm that the InSAR model with a uniform elastic structure (i.e., the REF model) fits the vertical GNSS data well (Figure 3c), indicating the consistency between InSAR and vertical GNSS observations. However, it predicts systematically lower horizontal displacements than the GNSS observations (Figure 3b). Importantly, inclusion of the weak channel in our models clearly improves the fit of horizontal GNSS data, particularly for the four stations immediately above the main rupture zone, without deteriorating the vertical GNSS data fit (Figures 3b and 3c). The optimal elastic parameters of the weak layer inferred from the GNSS data fit to our simple models (μ of 4 GPa and ν of 0.45) (Figure 3a) are highly compliant and equivalent to $V_p = 4.69$ km/s, $\frac{V_p}{V_c}$ = 3.32 when assuming a density of 2,000 kg/m³. $\frac{V_p}{V_c}$ ratios that can exceed 3.0 and ν ratios of up to 0.45 have been proposed based on seismic observations of the low velocity zone atop the slab in subduction zones (Audet & Bürgmann, 2014; Audet et al., 2009; Hansen et al., 2012; compilation in Tewksbury-Christle & Behr, 2021). Since high $\frac{V_P}{V}$ values are related to high porosity (Arnold et al., 1996), our results indicate that the weak layer may not only be weak in terms of strength but also have high porosity and pore pressure (Peacock et al., 2011). ν and $\frac{V_{\nu}}{V_{\nu}}$ ratios we estimate from geodetic modeling fall within the high range of values determined seismically for slab low-velocity layers, which tend to range between 2–3 for $\frac{V_P}{V_S}$ and 0.27–0.45 for ν . X. Q. Wang et al. (2012) demonstrate through experimental and modeling work that the combination of anisotropy and high pore fluid pressure can significantly raise $\frac{V_p}{V}$, a plausible scenario in our case given the observed seismic anisotropy. Deformation within a layer tends to be localized, while seismic waves sense bulk elastic moduli, which may also explain why values estimated from deformation result a slightly weaker layer than what seismic velocities suggest.

Although InSAR and GNSS data both require a lower rigidity (<30 GPa) of the weak layer than its surrounding bodies, the optimal range of rigidity for fitting the InSAR (>~12 GPa) is significantly higher than that for the (horizontal) GNSS data (~4 GPa) (Figure 3d). We interpret this discrepancy as possible evidence of mechanical anisotropy of the weak layer, that is, it has a higher strength in the vertical orientation than the horizontal. We acknowledge that this interpretation does not involve running anisotropic deformation models due to technical limitations. These geodetic findings are consistent with the seismic imaging in a geologic perspective.

LI ET AL. 7 of 13

1944/8007, 2024, 16, Downloaded from https://agupubs.onlinelibrary.wiley.com/doi/10.1029/2024GL110222, Wiley Online Library on [26/08/2024]. See the Terms and Conditions (https://onlinelibrary.wiley.com/terms-and-conditions) on Wiley Online Library for rules of use; OA articles are governed by the applicable Creative Commons Licensia.

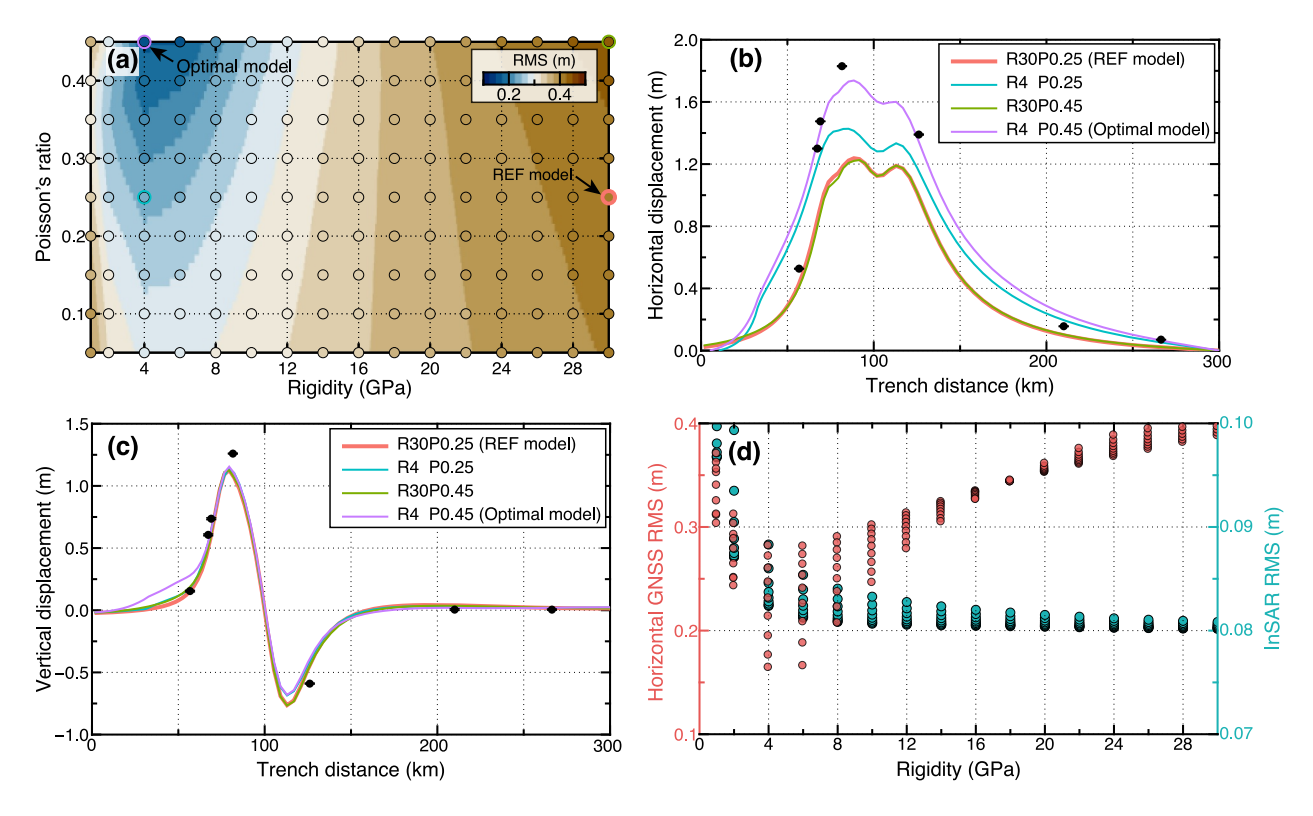


Figure 3. High compliance and strain anisotropy of the MHT inferred from geodetical modeling of GNSS and InSAR data. (a) Overall misfit of the horizontal GNSS data of all the isotropic weak-layer inverse models. (b) and (c) Four specific examples (denoted in (a) with circles of the same color codes) of the weak-layer models fitting the horizontal and vertical GNSS observations (black dots with error bars—the latter are small and hence lie within the dots). In the legend, R and P represent rigidity and Poisson's ratio, respectively, and numbers denote the two parameter values for each model. (d) Root-mean-square misfit of horizontal GNSS and InSAR (including three different looking angles) data of all weak-layer models plotted as a function of the weak-layer rigidity. Lower rigidity of weak-layer models is preferred in the horizontal direction (~4 GPa) than in the vertical direction (>12 GPa).

4. Further Discussion

4.1. Implications for Earthquake Cycle and Dynamics of Plate Margins

Broadly, earthquake-cycle (i.e., coseismic, postseismic, and interseismic) deformation (e.g., Li & Chen, 2023) have been extensively modeled to infer Earth bulk rheological structure and properties, such as layering in the Earth (Hearn & Bürgmann, 2005; Simons et al., 2002), 3D heterogeneity of elastic properties (Li & Barnhart, 2020; Puel et al., 2024; Tung & Masterlark, 2016; K. Wang & Fialko, 2018; Williams & Wallace, 2015), and lateral viscoelastic structural variations at subduction zones (Hsu et al., 2011; Li & Chen, 2022, 2023; Luo & Wang, 2021; Pollitz, 1996). Although fault slip is thought to be dominantly accommodated by a thin (tens of centimeters) fault core (Ben-Zion & Sammis, 2003), a compliant fault zone that is much thicker (kilometer scale) may constitute the plate boundary interface from field observations of exhumed ancient subduction faults (Agard et al., 2018; Bachmann et al., 2009; Oncken et al., 2022) and recently from seismological observations of a modern active subduction fault (Chalumeau et al., 2024). For strike-slip fault cases, compliant structure has been extensively studied with geodetic constraints (Barbot et al., 2008; Chen & Freymueller, 2002; Materna & Bürgmann, 2016; Xu et al., 2023). However, for megathrust faults at subduction/collision zones, most geodetic earthquake-cycle models assume the fault interface as a zero-thickness boundary and ignore the thickness of the weak zone for simplicity.

Our geodetic modeling results show that ignoring this structure, supported by seismological observations, systematically underestimates the geodetically determined coseismic slip of the fault and yields a different slip pattern (Figure S14 in Supporting Information S1). The cause of higher slip from the weak-layer models is that the deformation is more strongly confined to the vicinity of the layer, with less displacement transferred to the surface (Figures S19 and S20 in Supporting Information S1). Therefore, models with a weak zone require more slip along the fault than the models without such a weak zone to produce the same amount of deformation on the surface.

LI ET AL. 8 of 13

1944/807, 2024, 16, Dowloaded from https://agupubs.on/inelibrary.wiley.com/doi/10.1029/2024GL110222, Wiley Online Library on [26/082024]. See the Terms and Conditions (https://onlinelibrary.wiley.com/terms-and-conditions) on Wiley Online Library for rules of use; OA articles are governed by the applicable Creative Commons Licensia.

Figure 4. Conceptual interpretive sketch inferred from seismic imaging and geodetic modeling. Top surface shows topography for an area from the western boundary of the map in Figure 1a to just east of the HICLIMB dense line (cubes are stations), viewed from the East. Red surface lines are (from south to north) MFT, MBT, MCT (Lavé & Avouac, 2000), with fault cross sections symbolized by curved black lines. Pink shading indicates the Gorkha rupture outline from Mencin et al. (2016). Black circles show a conceptual zoom on sheet silicate fabric in the MHT layer with north dipping foliation planes (gray lines) that are elastically strong and seismically fast (blue arrows). In the perpendicular orientation, the layer is elastically weak and seismically slow (red arrows). For viscous deformation, layers parallel to foliation form weak planes (orange arrow). In the near field (MFT to the northern extent of Gorkha rupture), the upper plate accretionary wedge has similar elastic properties (short blue lines), possibly due to thrust faulting and folding. In the far field to the north, the geodetic solutions prefer mechanical weakness limited to the MHT channel.

Our forward simulations demonstrate that 3D models without a weak layer also underpredict the horizontal displacements (Text S4 in Supporting Information S1) and hence potentially obtain less fault slip and require more spatially varying fault geometry. Similarly, when omitting a weak zone, estimation of accumulated slip deficit during the interseismic phase and afterslip during the postseismic phase are also lower. Revisiting previous studies that did not consider a weak zone in terms of the release and accumulation of the slip deficit budget along the fault over earthquake cycles and associated assessment of earthquake hazards may be appropriate.

We demonstrate that mechanical anisotropy of a weak layer can be a solution to the discrepancy in optimal elastic properties from InSAR versus GNSS data (Figure 3d) without the need for added geometric complexity as required in previous studies. Such strain anisotropy is not a hitherto well recognized source of the non-uniqueness of earthquake source determination in previous studies. Strain anisotropy may lead to a dependence of determined fault slip in isotropic models on the data availability in horizontal and/or vertical components (Li & Chen, 2022). Consequently, our findings highlight the importance of geodetically monitoring both horizontal and vertical earthquake-cycle deformation for a better understanding of kinematics and dynamics at both continental collision and subduction zones.

4.2. Geologic Origins of MHT Anisotropy

Previous interpretations of seismic images suggested a low-velocity channel associated with the MHT, interpreted as the subducting sediment layer (Duputel et al., 2016; Nábělek et al., 2009), which motivated our weak channel models. Our finding of elastic anisotropy preferred by coseismic geodetic modeling was unexpected but aligns with azimuthal variations in receiver function conversions that also require anisotropy. We interpret the geodetic and seismic results in the following manner. Geodetic modeling prefers an MHT layer with higher rigidity in the vertical than in the horizontal. The receiver function azimuthal patterns require a contrast in foliation, where the foliation dips to the north or south, depending on whether the contrast is at the top or at the bottom of the more highly anisotropic layer and whether the anisotropy is best approximated by a fast or slow symmetry axis (Levin & Park, 1998; Schulte-Pelkum et al., 2020). In a top-to-the-south shear setting such as the MHT, foliation in a sheared layer is expected to dip north (Figure 4). The subducting plate is expected to contain sheet silicates with foliation planes that contain the seismically fast and elastically strong plane (Figure 4). To fulfill the geodetic condition of higher vertical than horizontal strength, the foliation planes would have to dip steeper than 45°. Although foliation with significant strain should align parallel to the gently dipping MHT, S-C fabrics can generate a dominant steeply dipping fast plane of anisotropy, at a high angle to the shear and tilted down to the north in this setting of top-to-the-south shear. An alternative possibility is strain localization on narrow MHT-

LI ET AL. 9 of 13



Acknowledgments

We thank the PIs and field teams of the

HICLIMB, NAMASTE, HIMNT, and

Harley Benz for internal reviews. This

work was supported by the Strategy Priority Research Program (Category B) of

(XDB0710000), the National Natural

Science Foundation of China (Grant

42288201) and U.S. National Science

1344582, and 2049743). We thank Roland

Bürgmann and an anonymous reviewer for

Foundation awards (EAR 1645009.

their constructive comments and

suggestions.

Chinese Academy of Sciences

GNSS deployments and Kelin Wang and

Geophysical Research Letters

10.1029/2024GL110222

parallel interfaces surrounded by broader high-angle fabric (Fossen, 2016). Such a geometry matches both the geodetic and seismic observations.

5. Conclusions

Seismic imaging of the MHT suggests a low-velocity channel associated with the plate interface. A channel with low seismic wave velocity is likely also mechanically weak. Such a feature is not typically incorporated in coseismic deformation modeling to date. At the same time, receiver functions show strong azimuthal variations that require anisotropy contrasts near the plate interface. When modeling of the coseismic deformation signal from the Gorkha GNSS and InSAR data, we find that including the weak layer improves particularly the fit of horizontal displacements over a homogeneous model. Both geodetic modeling and seismic imaging suggest a weak layer that is weaker in the horizontal orientation and stronger in the vertical orientation. We propose that such a weak layer together with laterally varying fault slip and geometry in a 3D context should be further explored in collision and subduction zones.

Data Availability Statement

Seismic data were accessed via the Incorporated Research Institutions for Seismology's Data Center funded through the Seismological Facilities for the Advancement of Geoscience (SAGE) Award of the National Science Foundation under Cooperative Support Agreement EAR-1851048 for the networks (Karplus et al., 2020; Nábělek, 2002; Sheehan et al., 2001). All geodetic data used in this work have been previously published (Galetzka et al., 2015; Hayes et al., 2015; Lindsey et al., 2015; McNamara et al., 2017; Wu et al., 2016; Yadav et al., 2017) and can be accessed at these publications, https://topex.ucsd.edu/nepal/ and http://geodesy.unr.edu. The used GNSS and InSAR data are also available at Li et al. (2024). All numerical simulations are performed using the PyLith software, which is available at Aagaard et al. (2019).

References

Aagaard, B., Knepley, M., & Williams, C. (2019). PyLith: A finite-element code for modeling quasi-static and dynamic crustal deformation. Geodynamics/pylith v2.2.2 (v2.2.2). Zenodo. https://doi.org/10.5281/zenodo.3269486

Aagaard, B., Knepley, M. G., & Williams, C. A. (2013). A domain decomposition approach to implementing fault slip in finite-element models of quasi-static and dynamic crustal deformation. *Journal of Geophysical Research: Solid Earth*, 118(6), 3059–3079. https://doi.org/10.1002/jgrb. 50217

Ader, T., Avouac, J.-P., Liu-Zeng, J., Lyon-Caen, H., Bollinger, L., Galetzka, J., et al. (2012). Convergence rate across the Nepal Himalaya and interseismic coupling on the Main Himalayan Thrust: Implications for seismic hazard. *Journal of Geophysical Research*, 117(B4). https://doi.org/10.1029/2011jb009071

Agard, P., Plunder, A., Angiboust, S., Bonnet, G., & Ruh, J. (2018). The subduction plate interface: Rock record and mechanical coupling (from long to short timescales). Lithos. 320. 537–566. https://doi.org/10.1016/j.lithos.2018.09.029

Arnold, M., Boccaccini, A., & Ondracek, G. (1996). Prediction of the Poisson's ratio of porous materials. *Journal of Materials Science*, 31(6), 1643–1646. https://doi.org/10.1007/bf00357876

Audet, P., Bostock, M. G., Christensen, N. I., & Peacock, S. M. (2009). Seismic evidence for overpressured subducted oceanic crust and megathrust fault sealing. *Nature*, 457(7225), 76–78. https://doi.org/10.1038/nature07650

Audet, P., & Bürgmann, R. (2014). Possible control of subduction zone slow-earthquake periodicity by silica enrichment. *Nature*, 510(7505), 389–392. https://doi.org/10.1038/nature13391

Avouac, J.-P. (2015). Mountain building: From earthquakes to geologic deformation. *Treatise on Geophysics*, 381–432. https://doi.org/10.1016/b978-0-444-53802-4.00120-2

Avouac, J.-P., Meng, L., Wei, S., Wang, T., & Ampuero, J.-P. (2015). Lower edge of locked Main Himalayan Thrust unzipped by the 2015 Gorkha earthquake. *Nature Geoscience*, 8(9), 708–711. https://doi.org/10.1038/ngeo2518

Bachmann, R., Oncken, O., Glodny, J., Seifert, W., Georgieva, V., & Sudo, M. (2009). Exposed plate interface in the European Alps reveals fabric styles and gradients related to an ancient seismogenic coupling zone. *Journal of Geophysical Research*, 114(B5). https://doi.org/10.1029/

Barbot, S., Fialko, Y., & Sandwell, D. (2008). Effect of a compliant fault zone on the inferred earthquake slip distribution. *Journal of Geophysical Research*, 113(B6). https://doi.org/10.1029/2007jb005256

Ben-Zion, Y., & Sammis, C. G. (2003). Characterization of fault zones. Pure and Applied Geophysics, 160, 677–715. https://doi.org/10.1007/978-3-0348-8010-7_11

Bilham, R. (2019). Himalayan earthquakes: A review of historical seismicity and early 21st century slip potential. *Geological Society, London, Special Publications*, 483(1), 423–482. https://doi.org/10.1144/sp483.16

Bilham, R., Gaur, V. K., & Molnar, P. (2001). Himalayan seismic hazard. Science, 293(5534), 1442–1444. https://doi.org/10.1126/science. 1062584

Bollinger, L., Avouac, J. P., Cattin, R., & Pandey, M. R. (2004). Stress buildup in the Himalaya. *Journal of Geophysical Research*, 109(B11). https://doi.org/10.1029/2003ib002911

Brownlee, S. J., Schulte-Pelkum, V., Raju, A., Mahan, K., Condit, C., & Orlandini, O. F. (2017). Characteristics of deep crustal seismic anisotropy from a compilation of rock elasticity tensors and their expression in receiver functions. *Tectonics*, 36(9), 1835–1857. https://doi.org/10.1002/2017tc004625

LI ET AL. 10 of 13

- Bürgmann, R., Kogan, M. G., Steblov, G. M., Hilley, G., Levin, V. E., & Apel, E. (2005). Interseismic coupling and asperity distribution along the Kamchatka subduction zone. *Journal of Geophysical Research*, 110(B7). https://doi.org/10.1029/2005jb003648
- Chalumeau, C., Agurto-Detzel, H., Rietbrock, A., Frietsch, M., Oncken, O., Segovia, M., & Galve, A. (2024). Seismological evidence for a multifault network at the subduction interface. *Nature*, 628(8008), 558–562. https://doi.org/10.1038/s41586-024-07245-y
- Chen, Q., & Freymueller, J. T. (2002). Geodetic evidence for a near-fault compliant zone along the San Andreas fault in the San Francisco Bay area. *Bulletin of the Seismological Society of America*, 92(2), 656–671. https://doi.org/10.1785/0120010110
- Dal Zilio, L., Hetényi, G., Hubbard, J., & Bollinger, L. (2021). Building the Himalaya from tectonic to earthquake scales. Nature Reviews Earth and Environment, 2(4), 251–268. https://doi.org/10.1038/s43017-021-00143-1
- Dielforder, A., Hetzel, R., & Oncken, O. (2020). Megathrust shear force controls mountain height at convergent plate margins. *Nature*, 582(7811), 225–229. https://doi.org/10.1038/s41586-020-2340-7
- Duputel, Z., Vergne, J., Rivera, L., Wittlinger, G., Farra, V., & Hetényi, G. (2016). The 2015 Gorkha earthquake: A large event illuminating the Main Himalayan Thrust fault. *Geophysical Research Letters*, 43(6), 2517–2525. https://doi.org/10.1002/2016gl068083
- Elliott, J., Jolivet, R., González, P. J., Avouac, J.-P., Hollingsworth, J., Searle, M., & Stevens, V. (2016). Himalayan megathrust geometry and relation to topography revealed by the Gorkha earthquake. *Nature Geoscience*, 9(2), 174–180. https://doi.org/10.1038/ngeo2623
- Feng, G., Li, Z., Shan, X., Zhang, L., Zhang, G., & Zhu, J. (2015). Geodetic model of the 2015 April 25 M_w 7.8 Gorkha Nepal Earthquake and M_W 7.3 aftershock estimated from InSAR and GPS data. *Geophysical Journal International*, 203(2), 896–900. https://doi.org/10.1093/gji/ggy335
- Feng, W., Lindsey, E., Barbot, S., Samsonov, S., Dai, K., Li, P., et al. (2017). Source characteristics of the 2015 M_w 7.8 Gorkha (Nepal) earthquake and its M_w 7.2 aftershock from space geodesy. *Tectonophysics*, 712, 747–758. https://doi.org/10.1016/j.tecto.2016.02.029Fossen, H. (2016). Structural geology. Cambridge University Press.
- Galetzka, J., Melgar, D., Genrich, J. F., Geng, J., Owen, S., Lindsey, E. O., et al. (2015). Slip pulse and resonance of the Kathmandu basin during the 2015 Gorkha earthquake, Nepal [Dataset]. Science, 349(6252), 1091–1095. https://doi.org/10.1126/science.aac6383
- Grandin, R., Vallée, M., Satriano, C., Lacassin, R., Klinger, Y., Simoes, M., & Bollinger, L. (2015). Rupture process of the Mw = 7.9 2015 Gorkha earthquake (Nepal): Insights into Himalayan megathrust segmentation. *Geophysical Research Letters*, 42(20), 8373–8382. https://doi.org/10.1002/2015GI 066044
- Hansen, R. T., Bostock, M. G., & Christensen, N. I. (2012). Nature of the low velocity zone in Cascadia from receiver function waveform inversion. Earth and Planetary Science Letters, 337, 25–38. https://doi.org/10.1016/j.epsl.2012.05.031
- Hayes, G. P., Briggs, R. W., Barnhart, W. D., Yeck, W. L., McNamara, D. E., Wald, D. J., et al. (2015). Rapid characterization of the 2015 M w 7.8 Gorkha, Nepal, earthquake sequence and its seismotectonic context [Dataset]. Seismological Research Letters, 86(6), 1557–1567. https://doi.org/10.1785/0220150145
- Hearn, E. H., & Bürgmann, R. (2005). The effect of elastic layering on inversions of GPS data for coseismic slip and resulting stress changes: Strike-slip earthquakes. *Bulletin of the Seismological Society of America*, 95(5), 1637–1653. https://doi.org/10.1785/0120040158
- Hetényi, G., Cattin, R., & Vergne, J. (2010). Geodynamics of Tibet and the Himalayas: Geophysical advances from imaging and modelling. Lambert Academic Publishing.
- Hodges, K. V. (2000). Tectonics of the Himalaya and southern Tibet from two perspectives. *Geological Society of America Bulletin*, 112(3), 324–350. https://doi.org/10.1130/0016-7606(2000)112<0324:tothas>2.3.co;2
- Hsu, Y.-J., Simons, M., Williams, C., & Casarotti, E. (2011). Three-dimensional FEM derived elastic Green's functions for the coseismic deformation of the 2005 Mw8.7 Nias-Simeulue, Sumatra earthquake. Geochemistry, Geophysics, Geosystems, 12(7). https://doi.org/10.1029/ 2011gc003553
- Jaeger, J. C., Cook, N. G., & Zimmerman, R. (2009). Fundamentals of rock mechanics. John Wiley and Sons.
- Jones, C. H., & Phinney, R. A. (1998). Seismic structure of the lithosphere from teleseismic converted arrivals observed at small arrays in the southern Sierra Nevada and vicinity, California. *Journal of Geophysical Research*, 103(B5), 10065–10090. https://doi.org/10.1029/97jb03540
- Kapp, P., & DeCelles, P. G. (2019). Mesozoic–Cenozoic geological evolution of the Himalayan-Tibetan orogen and working tectonic hypotheses. American Journal of Science, 319(3), 159–254. https://doi.org/10.2475/03.2019.01
- Karplus, M. S., Pant, M., Sapkota, S. N., Nábělek, J., Velasco, A. A., Adhikari, L. B., et al. (2020). A rapid response network to record aftershocks of the 2015 M 7.8 Gorkha earthquake in Nepal [Dataset]. Seismological Research Letters, 91(4), 2399–2408. https://doi.org/10.7914/XQ
- Lavé, J., & Avouac, J.-P. (2000). Active folding of fluvial terraces across the Siwaliks Hills, Himalayas of central Nepal. *Journal of Geophysical Research*, 105(B3), 5735–5770. https://doi.org/10.1029/1999jb900292
- Levin, V., & Park, J. (1998). P-SH conversions in layered media with hexagonally symmetric anisotropy: A cookbook. In Paper presented at the Geodynamics of Lithosphere & Earth's Mantle: Seismic Anisotropy as a Record of the Past and Present Dynamic Processes.
- Li, S., & Barnhart, W. D. (2020). Impacts of topographic relief and crustal heterogeneity on coseismic deformation and inversions for fault geometry and slip: A case study of the 2015 Gorkha earthquake in the Central Himalayan Arc. *Geochemistry, Geophysics, Geosystems*, 21(12), e2020GC009413. https://doi.org/10.1029/2020gc009413
- Li, S., & Chen, L. (2022). Elastic slab in viscoelastic mantle: Effects on determining megathrust slip and mantle viscosity during postseismic and interseismic phases. *Journal of Geophysical Research: Solid Earth*, 127(8), e2022JB024730. https://doi.org/10.1029/2022jb024730
- Li, S., & Chen, L. (2023). How long can the postseismic and interseismic phases of great subduction earthquake sustain? Toward an integrated earthquake-cycle perspective. *Geophysical Research Letters*, 50(11). https://doi.org/10.1029/2023gl103976
- Li, S., Schulte-Pelkum, V., Barnhart, W. D., Chen, L., Karplus, M., & Oncken, O. (2024). Weak, vertically stronger Main Himalayan Thrust in the India-Asia collision [Dataset]. Zenodo. https://doi.org/10.5281/zenodo.12696571
- Ligorría, J. P., & Ammon, C. J. (1999). Iterative deconvolution and receiver-function estimation. *Bulletin of the Seismological Society of America*, 89(5), 1395–1400. https://doi.org/10.1785/bssa0890051395
- Lindsey, E. O., Natsuaki, R., Xu, X., Shimada, M., Hashimoto, M., Melgar, D., & Sandwell, D. T. (2015). Line-of-sight displacement from ALOS-2 interferometry: Mw 7.8 Gorkha earthquake and Mw 7.3 aftershock [Dataset]. Geophysical Research Letters, 42(16), 6655–6661. https://doi.org/10.1002/2015GL065385
- Luo, H., & Wang, K. (2021). Postseismic geodetic signature of cold forearc mantle in subduction zones. *Nature Geoscience*, 14(2), 104–109. https://doi.org/10.1038/s41561-020-00679-9
- Masterlark, T. (2003). Finite element model predictions of static deformation from dislocation sources in a subduction zone: Sensitivities to homogeneous, isotropic, Poisson-solid, and half-space assumptions. *Journal of Geophysical Research*, 108(B11). https://doi.org/10.1029/2002jb002296
- Materna, K., & Bürgmann, R. (2016). Contrasts in compliant fault zone properties inferred from geodetic measurements in the San Francisco Bay area. *Journal of Geophysical Research: Solid Earth*, 121(9), 6916–6931. https://doi.org/10.1002/2016jb013243

LI ET AL. 11 of 13



Geophysical Research Letters

- 10.1029/2024GL110222
- McNamara, D. E., Yeck, W. L., Barnhart, W. D., Schulte-Pelkum, V., Bergman, E., Adhikari, L., et al. (2017). Source modeling of the 2015 Mw 7.8 Nepal (Gorkha) earthquake sequence: Implications for geodynamics and earthquake hazards [Dataset]. *Tectonophysics*, 714, 21–30. https://doi.org/10.1016/j.tecto.2016.08.004
- Mencin, D., Bendick, R., Upreti, B. N., Adhikari, D. P., Gajurel, A. P., Bhattarai, R. R., et al. (2016). Himalayan strain reservoir inferred from limited afterslip following the Gorkha earthquake. *Nature Geoscience*, 9(7), 533–537. https://doi.org/10.1038/ngeo2734
- Nábělek, J. (2002). Collaborative research: Lithospheric scale dynamics of active mountain building along the Himalayan-Tibetan collision zone [Dataset]. *International Federation of Digital Seismograph Networks. Dataset/Seismic Network*. https://doi.org/10.7914/SN/XF
- Nábělek, J., Hetényi, G., Vergne, J., Sapkota, S., Kafle, B., Jiang, M., et al. (2009). Underplating in the Himalaya-Tibet collision zone revealed by the Hi-CLIMB experiment. Science, 325(5946), 1371–1374. https://doi.org/10.1126/science.1167719
- Oncken, O., Angiboust, S., & Dresen, G. (2022). Slow slip in subduction zones: Reconciling deformation fabrics with instrumental observations and laboratory results. *Geosphere*, 18(1), 104–129. https://doi.org/10.1130/ges02382.1
- Park, J., & Levin, V. (2016). Anisotropic shear zones revealed by backazimuthal harmonics of teleseismic receiver functions. In Geophysical supplements to the monthly notices of the Royal Astronomical Society (Vol. 207, pp. 1216–1243). https://doi.org/10.1093/gji/ggw323
- Peacock, S. M., Christensen, N. I., Bostock, M. G., & Audet, P. (2011). High pore pressures and porosity at 35 km depth in the Cascadia subduction zone. Geology, 39(5), 471–474. https://doi.org/10.1130/g31649.1
- Pollitz, F. F. (1996). Coseismic deformation from earthquake faulting on a layered spherical Earth. *Geophysical Journal International*, 125(1), 1–14. https://doi.org/10.1111/j.1365-246x.1996.tb06530.x
- Puel, S., Becker, T. W., Villa, U., Ghattas, O., & Liu, D. (2024). Volcanic arc rigidity variations illuminated by coseismic deformation of the 2011 Tohoku-oki M9. Science Advances, 10(23), eadl4264. https://doi.org/10.1126/sciadv.adl4264
- Qiu, Q., Hill, E. M., Barbot, S., Hubbard, J., Feng, W., Lindsey, E. O., et al. (2016). The mechanism of partial rupture of a locked megathrust: The role of fault morphology. *Geology*, 44(10), 875–878. https://doi.org/10.1130/g38178.1
- Savage, M. K. (1998). Lower custal anisotropy or disping boundaries? Effects on receiver functions and a case study in New Zealand. *Journal of Conditional Proceedings* 1, 163077, 1500
- Geophysical Research, 103(B7), 15069–15087. https://doi.org/10.1029/98jb00795
 Schulte-Pelkum, V., & Mahan, K. H. (2014). A method for mapping crustal deformation and anisotropy with receiver functions and first results
- from USArray. Earth and Planetary Science Letters, 402, 221–233. https://doi.org/10.1016/j.epsl.2014.01.050 Schulte-Pelkum, V., Monsalve, G., Sheehan, A., Pandey, M., Sapkota, S., Bilham, R., & Wu, F. (2005). Imaging the Indian subcontinent beneath
- the Himalaya. *Nature*, 435(7046), 1222–1225. https://doi.org/10.1038/nature03678
 Schulte-Pelkum, V., Ross, Z. E., Mueller, K., & Ben-Zion, Y. (2020). Tectonic inheritance with dipping faults and deformation fabric in the brittle and ductile southern California crust. *Journal of Geophysical Research: Solid Earth*, 125(8), e2020JB019525. https://doi.org/10.1029/
- 2020jb019525
 Sheehan, A., Wu, F., & Bilham, R. (2001). Himalayan seismotectonics, Nepal and Tibet [Dataset]. *International Federation of Digital Seis-*
- mograph Networks. https://doi.org/10.7914/SN/YL
- Simons, M., Fialko, Y., & Rivera, L. (2002). Coseismic deformation from the 1999 Mw 7.1 Hector Mine, California, earthquake as inferred from InSAR and GPS observations. *Bulletin of the Seismological Society of America*, 92(4), 1390–1402. https://doi.org/10.1785/0120000933
- Tewksbury-Christle, C. M., & Behr, W. M. (2021). Constraints from exhumed rocks on the seismic signature of the deep subduction interface. Geophysical Research Letters, 48(18), e2021GL093831. https://doi.org/10.1029/2021gl093831
- Tung, S., & Masterlark, T. (2016). Coseismic slip distribution of the 2015 Mw 7. 8 Gorkha, Nepal, earthquake from joint inversion of GPS and InSAR data for slip within a 3-D heterogeneous Domain. *Journal of Geophysical Research: Solid Earth*, 121(5), 3479–3503. https://doi.org/10.1002/2015jb012497
- Wang, K., & Fialko, Y. (2015). Slip model of the 2015 Mw 7.8 Gorkha (Nepal) earthquake from inversions of ALOS-2 and GPS data. Geophysical Research Letters, 42(18), 7452–7458. https://doi.org/10.1002/2015g1065201
- Wang, K., & Fialko, Y. (2018). Observations and modeling of coseismic and postseismic deformation due to the 2015 Mw 7.8 Gorkha (Nepal) earthquake. *Journal of Geophysical Research: Solid Earth*, 123(1), 761–779. https://doi.org/10.1002/2017jb014620
- Wang, X. Q., Schubnel, A., Fortin, J., David, E. C., Guéguen, Y., & Ge, H. K. (2012). High Vp/Vs ratio: Saturated cracks or anisotropy effects? Geophysical Research Letters, 39(11). https://doi.org/10.1029/2012gl051742
- Williams, C. A., & Wallace, L. M. (2015). Effects of material property variations on slip estimates for subduction interface slow-slip events. Geophysical Research Letters, 42(4), 1113–1121. https://doi.org/10.1002/2014gl062505
- Wright, T. J., Parsons, B., England, P. C., & Fielding, E. J. (2004). InSAR observations of low slip rates on the major faults of western Tibet. Science, 305(5681), 236–239. https://doi.org/10.1126/science.1096388
- Wu, Y., Jiang, Z., Liang, H., Chang, L., Chen, C., Zhu, S., et al. (2016). Coseismic deformations of the 2015 MW 7.8 Gorkha earthquake and interseismic strain accumulation in the Himalayan tectonic belt and Tibetan Plateau [Dataset]. Tectonophysics, 670, 144–154. https://doi.org/10.1016/j.tecto.2015.12.028
- Xu, X., Liu, D., & Lavier, L. (2023). Constraining fault damage zone properties from geodesy: A case study near the 2019 ridgecrest earthquake sequence. Geophysical Research Letters, 50(5), e2022GL101692. https://doi.org/10.1029/2022g1101692
- Yadav, R. K., Roy, P., Gupta, S. K., Khan, P., Catherine, J., Prajapati, S. K., et al. (2017). Rupture model of Mw 7.8 2015 Gorkha, Nepal earthquake: Constraints from GPS measurements of coseismic offsets [Dataset]. *Journal of Asian Earth Sciences*, 133, 56–61. https://doi.org/10.1016/j.jseaes.2016.04.015
- Yin, A. (2006). Cenozoic tectonic evolution of the Himalayan orogen as constrained by along-strike variation of structural geometry, exhumation history, and foreland sedimentation. *Earth-Science Reviews*, 76(1), 1–131. https://doi.org/10.1016/j.earscirev.2005.05.004
- Yin, A., & Harrison, T. M. (2000). Geologic evolution of the Himalayan-Tibetan orogen. Annual Review of Earth and Planetary Sciences, 28(1), 211–280. https://doi.org/10.1146/annurev.earth.28.1.211

References From the Supporting Information

- Abers, G. A. (2005). Seismic low-velocity layer at the top of subducting slabs: Observations, predictions, and systematics. *Physics of the Earth and Planetary Interiors*, 149(1–2), 7–29. https://doi.org/10.1016/j.pepi.2004.10.002
- Adhikari, L., Laporte, M., Bollinger, L., Vergne, J., Lambotte, S., Koirala, B., et al. (2023). Seismically active structures of the Main Himalayan Thrust revealed before, during and after the 2015 Mw 7.9 Gorkha earthquake in Nepal. *Geophysical Journal International*, 232(1), 451–471. https://doi.org/10.1093/gji/ggac281
- Audet, P., & Kim, Y. (2016). Teleseismic constraints on the geological environment of deep episodic slow earthquakes in subduction zone forearcs: A review. *Tectonophysics*, 670, 1–15. https://doi.org/10.1016/j.tecto.2016.01.005

LI ET AL. 12 of 13

- Behr, W. M., & Burgmann, R. (2021). What's down there? The structures, materials and environment of deep-seated slow slip and tremor. Philosophical Transactions of the Royal Society A, 379(2193), 20200218. https://doi.org/10.1098/rsta.2020.0218
- Bilham, R., Mencin, D., Bendick, R., & Bürgmann, R. (2017). Implications for elastic energy storage in the Himalaya from the Gorkha 2015 earthquake and other incomplete ruptures of the Main Himalayan Thrust. *Quaternary International*, 462, 3–21. https://doi.org/10.1016/j.quaint.
- Caldwell, W. B., Klemperer, S. L., Lawrence, J. F., Rai, S. S., & Ashish (2013). Characterizing the Main Himalayan Thrust in the Garhwal Himalaya, India with receiver function CCP stacking. *Earth and Planetary Science Letters*, 367, 15–27. https://doi.org/10.1016/j.epsl.2013.
- Calvert, A. J., Bostock, M. G., Savard, G., & Unsworth, M. J. (2020). Cascadia low frequency earthquakes at the base of an overpressured subduction shear zone. *Nature Communications*, 11(1), 3874. https://doi.org/10.1038/s41467-020-17609-3
- Diao, F., Wang, R., Xiong, X., & Liu, C. (2021). Overlapped postseismic deformation caused by afterslip and viscoelastic relaxation following the 2015 Mw 7.8 Gorkha (Nepal) earthquake. *Journal of Geophysical Research: Solid Earth*, 126(3), e2020JB020378. https://doi.org/10.1029/2020jb020378
- Fagereng, Å. (2011). Geology of the seismogenic subduction thrust interface. Geological Society, London, Special Publications, 359(1), 55–76. https://doi.org/10.1144/sp359.4
- Hong, S., & Liu, M. (2021). Postseismic deformation and afterslip evolution of the 2015 Gorkha earthquake constrained by InSAR and GPS observations. *Journal of Geophysical Research: Solid Earth*, 126(7), e2020JB020230. https://doi.org/10.1029/2020jb020230
- Hubbard, J., Almeida, R., Foster, A., Sapkota, S. N., Bürgi, P., & Tapponnier, P. (2016). Structural segmentation controlled the 2015 Mw 7.8 Gorkha earthquake rupture in Nepal. Geology, 44(8), 639–642. https://doi.org/10.1130/g38077.1
- Ingleby, T., Wright, T., Hooper, A., Craig, T., & Elliott, J. (2020). Constraints on the geometry and frictional properties of the Main Himalayan Thrust using coseismic, postseismic, and interseismic deformation in Nepal. *Journal of Geophysical Research: Solid Earth*, 125(2), e2019JB019201. https://doi.org/10.1029/2019jb019201
- Kang, H., & Kim, Y. (2019). Localized anisotropic subduction-zone structure in southern Peru: Constraints from teleseismic receiver functions and forward modeling. Seismological Research Letters, 90(5), 1820–1835. https://doi.org/10.1785/0220180384
- Kim, Y., Abers, G. A., Li, J., Christensen, D., Calkins, J., & Rondenay, S. (2014). Alaska Megathrust 2: Imaging the megathrust zone and Yakutat/Pacific plate interface in the Alaska subduction zone. *Journal of Geophysical Research: Solid Earth*, 119(3), 1924–1941. https://doi.org/10.1002/2013jb010581
- Liu-Zeng, J., Zhang, Z., Rollins, C., Gualandi, A., Avouac, J. P., Shi, H., et al. (2020). Postseismic deformation following the 2015 Mw7. 8 Gorkha (Nepal) earthquake: New GPS data, kinematic and dynamic models, and the roles of afterslip and viscoelastic relaxation. *Journal of Geophysical Research: Solid Earth*, 125(9), e2020JB019852. https://doi.org/10.1029/2020Jb019852
- Lohman, R. B., & Simons, M. (2005). Some thoughts on the use of InSAR data to constrain models of surface deformation: Noise structure and data downsampling. *Geochemistry, Geophysics, Geosystems*, 6(1). https://doi.org/10.1029/2004gc000841
- Mahan, K. (2006). Retrograde mica in deep crustal granulites: Implications for crustal seismic anisotropy. Geophysical Research Letters, 33(24). https://doi.org/10.1029/2006g1028130
- Monsalve, G., Sheehan, A., Rowe, C., & Rajaure, S. (2008). Seismic structure of the crust and the upper mantle beneath the Himalayas: Evidence for eclogitization of lower crustal rocks in the Indian plate. *Journal of Geophysical Research*, 113(B8), B08315. https://doi.org/10.1029/2007/IB005424
- Song, T.-R. A., Helmberger, D. V., Brudzinski, M. R., Clayton, R. W., Davis, P., Pérez-Campos, X., & Singh, S. K. (2009). Subducting slab ultraslow velocity layer coincident with silent earthquakes in southern Mexico. *Science*, 324(5926), 502–506. https://doi.org/10.1126/science.
- Zhang, J., Hu, Y., Zhao, B., & Chen, Y. (2023). Weakness of the Indian lower crust beneath the Himalaya inferred from postseismic deformation of the 2015 Mw 7.8 Gorkha earthquake. *Journal of Geophysical Research: Solid Earth*, 128(11), e2023JB027119. https://doi.org/10.1029/2023jb027119
- Zhao, B., Bürgmann, R., Wang, D., Tan, K., Du, R., & Zhang, R. (2017). Dominant controls of downdip afterslip and viscous relaxation on the postseismic displacements following the Mw 7. 9 Gorkha, Nepal, earthquake. *Journal of Geophysical Research: Solid Earth*, 122(10), 8376–8401. https://doi.org/10.1002/2017jb014366

LI ET AL. 13 of 13